IJAE
Vol. 124, n. 2: 230-246, 2019
ITALIAN JOURNAL OF ANATOMY AND EMBRYOLOGY

Research Article - Basic and Applied Anatomy

Situs inversus totalis in a 96-year-old female cadaver: evidence pointing toward the two-cilia model

Mia Jenkins, Andrey Frolov, Yun Tan, Daniel Daly, Craig Lawson, John R. Martin, III*

Center for Anatomical Science and Education, Department of Surgery, Saint Louis University School of Medicine, 1402 S. Grand Blvd., Schwitalla Hall M-306, St. Louis, Missouri, 63104, USA

Abstract

Situs inversus totalis is a complete transposition of the thoracic and abdominal organs and represents one of many laterality defects within the heterotaxy spectrum. Here we report a case of a 96-year-old female cadaver with situs inversus. Examination of the respective computed tomography images revealed situs inversus totalis with dextrocardia. A detailed dissection demonstrated the transposition of the viscera and confirmed complete reversal of the visceral organs without major anomalies. In order to gain insight into the etiology of the present anatomical anomaly, we performed a screen for the putative genetic variants in the coding regions (exomes) of the DNA extracted from the cadaveric tissue using Next Generation Sequencing (NGS) technology. The analysis of the data revealed the presence of genetic variants, *DVL1*, *DNAH9*, *PKD1*, and *TRPV4*, that are closely associated with the regulation of cilia structure and function. Aberrant cilia function has been proposed by other investigators to be a major cause of laterality defects. Because *DNAH9* mutation could be linked to the impairment of motile primary cilia function and mutations in *DVL1*, *PKD1*, and *TRPV4* to that of non-motile primary cilia, our data could provide evidence in support of the two-cilia model where a synergistic functioning of both cilia types is required for a proper activation of the asymmetrical Nodal cascade in the left lateral plate mesoderm thereby assuring a typical and complete asymmetrical patterning of visceral organs.

Keywords

Situs inversus totalis, dextrocardia, computed tomography, DNA exome sequencing, next generation sequencing, two-cilia model.

Introduction

Situs inversus represents a group of congenital disorders characterized by reversal of visceral organs along the left-right axis. It falls within the heterotaxy spectrum which defines the orientation of the visceral organs in the thorax and abdomen and includes situs solitus (normal), situs ambiguous (heterotaxy) and situs inversus totalis (reversed). The latter condition represents a complete mirrored image of situs solitus and has an incidence of 1 in 10,000 (Kim, 2011; Lin et al., 2014). In situs inversus totalis, the apex of the heart is pointed to the right (dextrocardia) with a bilobed right lung and a trilobed left lung in the thoracic cavity. The abdominal viscera are also reversed with the liver being located in the left upper quadrant and the stomach and spleen being located in the right upper quadrant of the abdominal cavity. It is

* Corresponding author. E-mail: john.martin@health.slu.edu

http://www.fupress.com/ijae
DOI: 10.13128/ijae-10794

well established that the disruption of the left-right axis, also called laterality, causes situs inversus totalis (Nonaka et al., 1998; Vandenberg and Levin, 2013; Blum et al., 2014) and dysfunctional cilia at the embryonic node is a major contributor to laterality defects (Nonaka et al., 1998; Yoshiba and Hamada, 2014; Pennekamp et al., 2015). The organ arrangement has been attributed to improper initiation by the primary and motile cilia of the leftward asymmetric genetic flow in the lateral plate mesoderm during gastrulation (Nonaka et al., 1998; Bisgrove and Yost, 2006; Fliegauf et al., 2007; Leigh et al., 2009; Pennekamp et al., 2015). The left-right asymmetrical distribution of visceral organs is one of the major biological processes underlying the normal development of the human body and gaining more insight into its molecular mechanism(s) would be very important for our better understanding and treatment of the pathologies associated with the incorrect left-right viscera patterning (Burton et al., 2014; Ekbote et al., 2014; Elder et al., 2014).

The purpose of this study is to describe the anatomical characteristics of situs inversus in a 96-year-old female cadaver as well as to identify novel genetic variants associated with the development of situs inversus in humans. To the best of our knowledge, this is the first comprehensive characterization of situs inversus in the human body which includes computed tomography (CT) imaging, gross anatomical examination, and genetic analysis.

Materials and Methods

Human cadaveric body procurement

A 96-year-old female cadaver was received through Saint Louis University (SLU) School of Medicine Gift Body Program from an individual who had given her written informed consent. The body was embalmed through the right femoral artery with a solution (2:1 ratio) of water and mixture containing 33.3% glycerin, 28.8% phenol, 4.6% formaldehyde, and 33.3% methanol. The medical record indicated a presence of situs inversus without further specification.

Computed tomography imaging

The cadaver underwent a CT scanning at SLU Hospital using Siemens SOMATOM Definition Flash system (140 kV; 119 mAs; slice thickness: 3 mm by 3 mm interval; detector size: 0.6 mm, 128 rows of detectors, pitch of 0.6). A total of 83 coronal, 397 axial, and 140 sagittal images were obtained with standard resolution and analyzed using Syngo Fast-View software to determine the type of situs inversus in the cadaveric body. An Interactive Atlas of Human Anatomy (IMAIOS) and Imaging Atlas of Human Anatomy (Weir et al., 2011) were used to assure a correct identification of the major viscera on the CT scans.

Anatomical dissection

Dissection procedures were conducted according to Casey and Campeau (2014) and Delton (2017). To that end, a Y-shaped incision was made to reflect the skin and

expose the underlying muscles, rib cage, parietal pleura, and peritoneum. The incision was made from the right and left clavicles to the midline of the body down to the superior surface of the pubic symphysis. After the skin was reflected, the muscles were removed from the rib cage and the ribs were cut by a Stryker saw along the midaxillary line of the thoracic wall from rib 10 to the clavicle and then to the sternum. The thoracic and abdominal viscera were examined and each dissection step was thoroughly documented using a Canon EOS 350D/ Digital Rebel XT camera.

Thorax

The great vessels of the neck and the right and left phrenic and vagus nerves were dissected before opening the pericardial sac. Once the pericardium was cut, reflected and cleaned, the major vasculature of the heart was exposed. The direction of the apex of the heart and the number of lobes on each lung were documented. The hila of the lungs were cut to remove the lungs from the thoracic cavity. The major vasculature and the bronchial tree were identified in the hilum of each lung. The great vessels of the heart were sectioned to remove the heart from the pericardial sac. Each functional chamber of the heart was cleaned and identified. The structures of the posterior mediastinum were dissected.

Abdomen

After major viscera, vasculature and nerves had been identified in the thoracic cavity, the abdominal structures were then examined. The diaphragm was cut in the midline and reflected to show all the borders of the liver. The portal triad was dissected and then cut midway at the hepatoduodenal ligament. The inferior vena cava and ligaments of the liver were cut to remove the liver and the vasculature and biliary system were then documented. Next, the three unpaired branches (celiac trunk, superior mesenteric artery and inferior mesenteric artery) from the abdominal aorta were cleaned and exposed. The vasculature of the entire digestive tract was cleaned and identified. The small intestines were reflected superiorly in order to view the abdominal aorta and inferior vena cava. Lastly, the kidneys and corresponding vasculature as well as the spleen were studied.

Genetic Analysis

Next Generation Sequencing (NGS) and bioinformatics analysis were performed as previously described (Frolov et al., 2018) with the following modifications. DNA was extracted from lung specimen procured from the embalmed human body and was sequenced to 30x depth of coverage (~4.5 Gb) on the Illumina HiSeq 2500 NGS platform. The 30x depth of coverage fulfills a requirement for the detection of human genome mutations (10x to 30x, Illumina). DNA extraction and exome sequencing were conducted by Omega Bioservices (Norcross, GA). The bioinformatics analysis (the variant calls and annotation of genetic variants) was performed by Genome Technology Access Center (GTAC) at Washington University in St. Louis. Genetic variants with deleterious (pathologic) amino acid substitutions were identified through the consecutive filtering steps described in Table 1. More specifically, *Step 1* allows

Table 1. Filtering steps to identify rare deleterious (pathologic) amino acid substitutions in mutant proteins associated with the present case of situs inversus.

Step 1	Remove synonymous, non-frameshift deletion, non-frameshift insertion, unknown, and not available (NA) variants.
Step 2	Remove variants in the ExAc 65,000 exomes with minor allele frequency (MAF) > 0.01.
Step 3	Keep SIFT-predicted, disease-associated (D) and NA variants.
Step 4	Keep PolyPhen_2-HDIV -predicted D, pathologic (P), and NA variants.
Step 5	Keep PROVEAN-predicted D and NA variants.

a removal of the genetic variants that will not change the encoded amino acid due to the degenerate nature of genetic code (synonymous mutation) or least likely to affect a correct transcription of the respective genes (non-frameshift deletion and non-frameshift insertion mutations) thereby not resulting in aberrant protein structures. *Step 2* is taking out of consideration a bulk of common genetic variants in human population. *Steps 3-5* select proteins with predicted deleterious (pathologic) amino acid substitutions by applying sequentially (to the genetic variants remaining after *Step 2*) a SWIFT (Sim et al. 2012), PolyPhen_2-HDIV (Adzhubei et al., 2010), and PROVEAN (Choi and Chan, 2015) algorithms. The UniProtKB Protein knowledgebase as well as the information extracted from the literature obtained through PubMed and Google Scholar database searches were used for the functional annotation of the resultant genetic variants (mutations).

Results

Anatomical characterization: CT imaging

From the 397 axial images obtained, 4 thoracic vertebral levels (TV2, TV3, TV5, and TV8) and 4 lumbar vertebral levels (LV1, LV2, LV4, and LV5) were chosen to document the major viscera and vasculature of the thorax and abdomen.

At the 2nd thoracic vertebral level (TV2), from anterior to posterior, the right and left brachiocephalic veins were identified deep to the sternum. The brachiocephalic trunk branched from the arch of the aorta on the left, while the right common carotid and right subclavian arteries branched independently on the right. The right and left lungs were identified on each side of the mediastinum with the trachea and esophagus located slightly left of the midline (Fig. 1).

At the 3rd thoracic vertebral level (TV3), the right brachiocephalic vein coursed obliquely to the left before it joined the left brachiocephalic vein to form the superior vena cava. The arch of the aorta was observed and extended from left to right. The trachea was posterior to the aortic arch and anterior to the esophagus (Fig. S1).

At the 5th thoracic vertebral level (TV5), the ascending aorta was posterior to the left side of the sternum and located to the left of the middle thoracic cavity. The azygos vein was located posteriorly and medially to the left-sided superior vena cava. The pulmonary trunk traveled posteriorly and slightly to the right of the arch of the

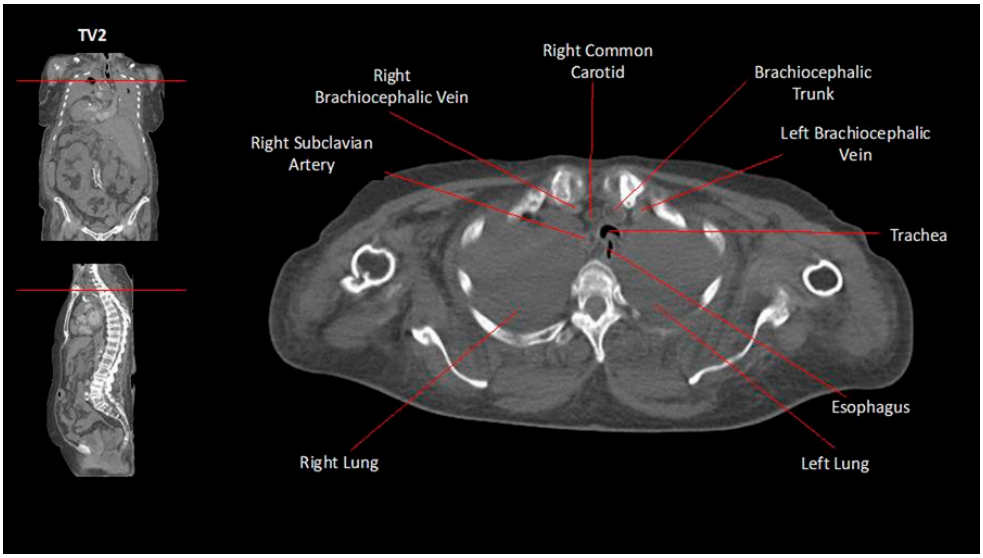

Figure 1. CT imaging of the great vessels of the superior mediastinum at the thoracic vertebral level 2 (TV 2). The right common carotid artery and right subclavian artery are identified as direct braches from the arch of the aorta and the brachiocephalic trunk is identified on the left. The red lines in the coronal and sagittal images denote the vertebral level.

aorta before branching into the left and right pulmonary arteries. The descending (thoracic) aorta was identified to the right of the vertebral column. The esophagus was to the left of the descending aorta (Fig. S2).

The chambers of the heart were identified at the 8th thoracic vertebral level (TV8), and the apex of the heart pointed to the right (dextrocardia). Both functional right atrium and ventricle were posterior to the sternum with the atrium located on the left side. The functional left atrium was anterior to the esophagus and the descending aorta was located to the right of the vertebral column. The functional left ventricle was identified with the outflow tract ending at the aortic valve (Fig. 2).

The major abdominal viscera were identified at the 1st lumbar vertebral level (LV1). On the left side of the abdomen, the liver was identified, while the stomach and spleen were located on the right side. The pancreas traversed the abdomen with the tail of the pancreas pointing to the hilum of the spleen. The left renal vein drained into the inferior vena cava on the left side of the vertebral column (Fig. 3). The right renal vein passed anterior to the abdominal aorta and drained into the inferior vena cava on the left at the 2nd lumbar vertebral level (LV2) (Fig. 4).

At the 4th lumbar vertebral level (LV4), the ascending colon and cecum were identified on the left side, while the descending colon was located on the right side of the abdomen. The right and left common iliac arteries bifurcated from the abdominal aorta (Fig. S3). The common iliac veins ran parallel to the common iliac arteries at the 5th lumbar vertebral level (LV5) before they joined to form the inferior vena cava (Fig. S4).

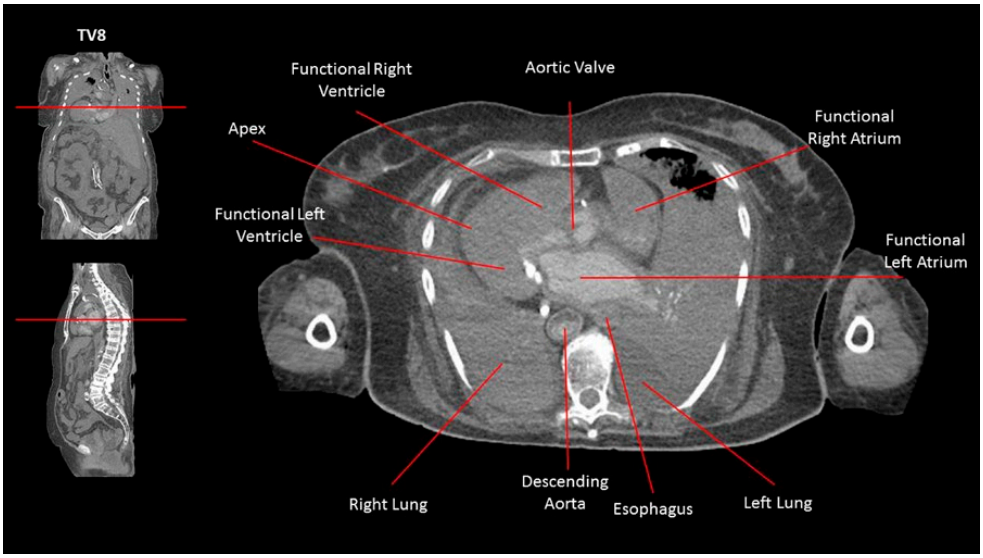

Figure 2. CT imaging of the heart chambers at the thoracic vertebral level 8 (TV 8). The functional right atrium and functional right ventricle are the most anterior chambers located posterior to the sternum. The functional left atrium is located just anterior to the descending aorta and esophagus. The functional left ventricle with its apex of the heart is directed towards the right. The descending aorta can be seen to the right of the vertebral column while the esophagus is located just left of the midline. The red lines in the coronal and sagittal images denote the vertebral level.

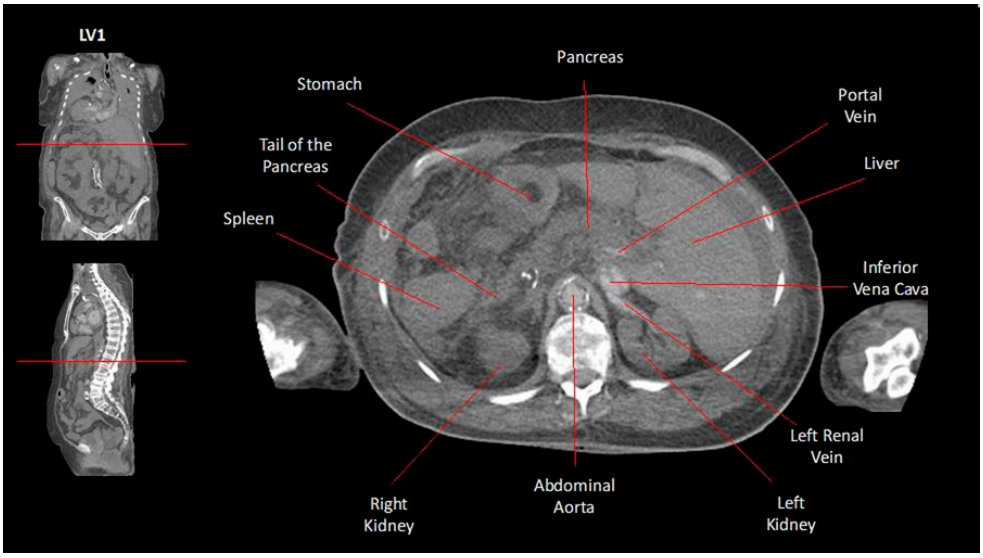

Figure 3. CT imaging of the abdominal viscera at the lumbar vertebral level 1 (LV1). The liver is located on the left side of the abdomen while the stomach and spleen are located on the right. The tail of the pancreas is toward the right. The inferior vena cava is to the left of the abdominal aorta and posterior to the liver. The red lines in the coronal and sagittal images denote the vertebral level.

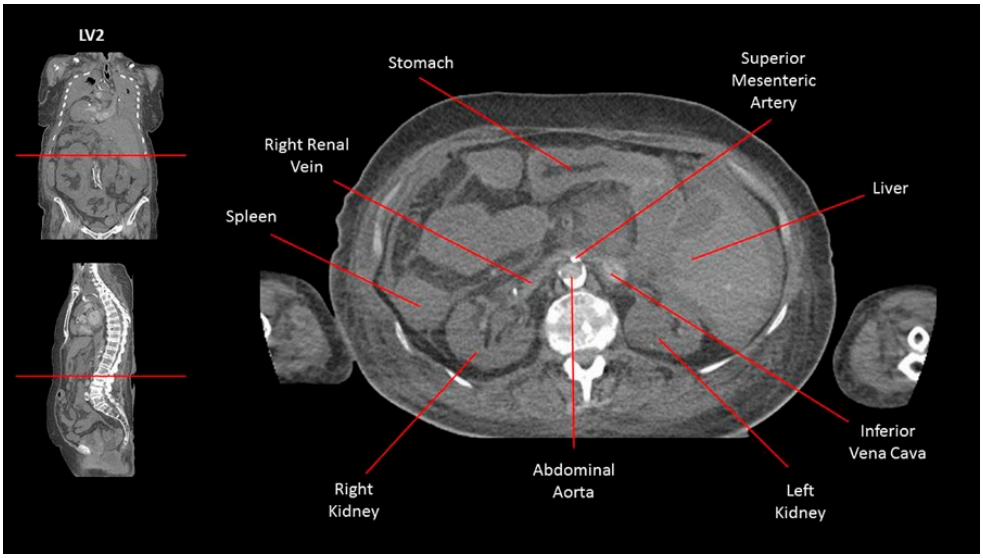

Figure 4. CT imaging of the right renal vein at the lumbar vertebral level 2 (LV2). The right renal vein passes anterior to the abdominal aorta and posterior to the superior mesenteric artery before draining into the inferior vena cava on the left side of the abdomen. The red lines in the coronal and sagittal images denote the vertebral level**.**

Anatomical characterization: Gross dissection

In the thoracic cavity, the cadaver presented with dextrocardia (apex of the heart pointing to the right) with a bilobed right lung and a trilobed left lung (Fig. 5). The right brachiocephalic vein traveled obliquely from the right side of the superior thorax to the left to join with the left brachiocephalic vein to form the left-sided superior vena cava. The superior vena cava then emptied into the functional right atrium. The aortic arch began anteriorly and ended posteriorly at the sternal angle level. The brachiocephalic trunk, right common carotid artery, and right subclavian artery branched from the arch of the aorta from left to right, respectively. The right and left phrenic nerves passed anterior to the hila of the lungs, and the left and right vagus nerves passed posterior to the hila of the lungs (Fig. S5).

The major vasculature of the heart was identified. The direct branches from the ascending aorta, the right and left coronary arteries, were identified in the coronary sulcus. From the anterior view of the heart, the left coronary artery gave off the left marginal artery at the inferior border of the heart. The anterior interventricular artery, a branch of the right coronary artery, was identified in the anterior interventricular sulcus traveling with the great cardiac vein towards the apex of the heart. From the posterior view of the heart, the continuation of the left coronary artery was viewed as it gave off the posterior interventricular branch which traveled with the middle cardiac vein in the posterior interventricular sulcus. The right circumflex artery wrapped around the right side of the heart in the coronary sulcus with the small cardiac vein

and ended before reaching the posterior aspect of the heart. The great, middle and small cardiac veins finally drained into the coronary sinus (Fig. S6).

The chambers of the heart were identified and were named based on function, not anatomical position. The chambers of the left side of the heart (left atrium and left ventricle) and the right side of the heart (right atrium and right ventricle) were named functional right atrium, functional right ventricle, functional left atrium, and functional left ventricle, respectively. Each functional chamber was found to have the characteristic structures typical of situs solitus (Fig. S7). The functional right atrium received venous blood from the superior vena cava, inferior vena cava, and coronary sinus. Within the chamber, pectinate muscles fanned out from the crista terminalis. The fossa ovalis was identified in the interatrial septum. Between the functional right atrium and functional right ventricle there was the tricuspid valve. Within the functional right ventricle, the anterior, posterior, and septal papillary muscles were identified with chordae tendineae connecting them to the cusps of the tricuspid valve. Trabeculae carneae were identified on the wall of the ventricle. The septum trabecula (moderator band) was identified, forming a bridge between the interventricular wall and the anterior papillary muscle. The conus arteriosus led into the pulmonary trunk toward the right. The functional left atrium received two pairs of the pulmonary veins from each side. The cusps of the mitral valve were observed between the functional left atrium and functional left ventricle. Finally, within the functional left ventricle, the anterior and posterior papillary muscles were connected to the cusps of the mitral valve by chordae tendineae. Trabeculae carneae were also identified on the wall of the functional left ventricle. The aortic vestibule ended at the aortic valve (Fig. S7).

Once the lungs were removed from the thoracic cavity, each hilum was examined. The right lung presented with two lobes, superior and inferior, separated by the oblique fissure. The lingula and the cardiac notch were located on the anterior border of the inferior part of the superior lobe. At the hilum of the right lung, the right pulmonary artery was superior, the primary bronchus was posterior, and the superior and inferior pulmonary veins were inferior. The left lung presented with three lobes. The oblique fissure separated the superior and middle lobes from the inferior lobe and the horizontal fissure separated the superior lobe from the middle lobe. At the hilum of the left lung, the left pulmonary artery, the primary bronchus, and the superior and inferior pulmonary veins had a similar arrangement to that of the right lung (Fig. S8).

In the posterior mediastinum, the left and right vagus nerves passed posterior to the hilum of the lungs and approached the esophagus where they contributed to the esophageal plexus. Towards the caudal end of the esophagus, the esophageal plexus narrowed and continued as the anterior and posterior vagal trunks where the right vagus nerve contributed to the anterior vagal trunk and the left vagus nerve contributed to the posterior vagal trunk. The azygos vein emptied into the superior vena cava on the left side of the thoracic cavity over the hilum of the right lung. The hemiazygos and accessory hemiazygos veins were found on the right side and both passed anterior to the vertebral bodies to the left side of the thorax, posterior to the esophagus at the TV9 level and TV8 level, respectively. The thoracic duct was identified between the descending aorta and azygos vein, and crossed to the right side at the level of TV5 and drained into the junction between the right jugular vein and right subclavian vein at the root of the neck (Fig. S9).

In the abdominal cavity, the liver was located in the left upper quadrant of the abdomen. The esophagus passed through the diaphragm at the TV10 level and ended at the cardiac notch of the stomach on the right side of the abdominal cavity (Fig. 5). The 1st part of the duodenum began its descent on the left side of the abdomen at the LV1 level, and crossed transversely to the opposite side at the LV3 level (Fig. 6). The jejunum primarily occupied the right upper quadrant and the ileum was mostly identified in the left lower quadrant of the abdomen with no sign of malrotation. The cecum was identified in the left lower quadrant, and it connected to the terminal ilium and continued as the ascending colon. The transverse colon began at the left colic flexure and traveled horizontally across to the right colic flexure where it became the descending colon. The sigmoid colon continued from the descending colon and traveled into pelvic cavity on the right side and ended at the rectum. A single spleen was located in the right upper quadrant inferior to the diaphragm.

The major paired/unpaired branches from the abdominal aorta were identified. The celiac trunk usually branches into three arteries, but in this study the celiac trunk bifurcated into the splenic artery and the right gastric artery (Fig. S10). The common hepatic artery shared a common trunk with the superior mesenteric artery. The right gastric artery traveled through the hepatogastric ligament to supply the lesser curvature of the stomach. The splenic artery traveled toward the spleen on the right side (Fig. S11). The common hepatic artery ran toward the left and gave off the inferior pancreaticoduodenal artery, gastroduodenal artery, and continued as the proper hepatic artery. The superior pancreaticoduodenal arteries branched from the gastroduodenal artery to provide blood supply to the head of the pancreas and duodenum. In this study, the inferior pancreaticoduodenal artery branched from the common hepatic artery to supply the same area as the superior pancreaticoduodenal artery (Fig. S12).

The portal triad, consisting of the portal vein, proper hepatic artery with an accessary hepatic artery in this case, and common bile duct, was identified in the hepatoduodenal ligament. The common bile duct joined with the major pancreatic duct and opened into the major papilla of the duodenum on the left side of the abdomen. The portal vein was formed by the splenic vein and the superior mesenteric vein dorsal to the neck of the pancreas. The proper hepatic artery gave off left and right hepatic arteries and an additional common trunk for an accessory hepatic artery and left gastric artery (Figs. S13 & S14). The right hepatic artery and accessory hepatic artery accompanied each other to the right functional lobe of the liver.

The branches of the superior mesenteric artery were also identified (Fig. S15). The intestinal arteries passed in the mesentery proper to supply the jejunum and ileum. The middle colic artery traveled through the transverse mesocolon to provide blood supply to the left two-thirds of the transverse colon. The left colic artery traveled retroperitoneally to provide blood supply to the ascending colon. Lastly, the ileocolic artery traveled inferiorly and laterally through the mesentery proper to the terminal ileum, cecum, and lower ascending colon on the left side in the abdominal cavity.

The branches from the inferior mesenteric artery were examined (Fig. S16). The right colic artery traveled retroperitoneally to supply the descending colon on the right side. The sigmoid branches traveled through the sigmoid mesocolon to supply the sigmoid colon. The inferior mesenteric artery continued as the superior rectal artery in the pelvic cavity to supply the superior portion of the rectum. Branches

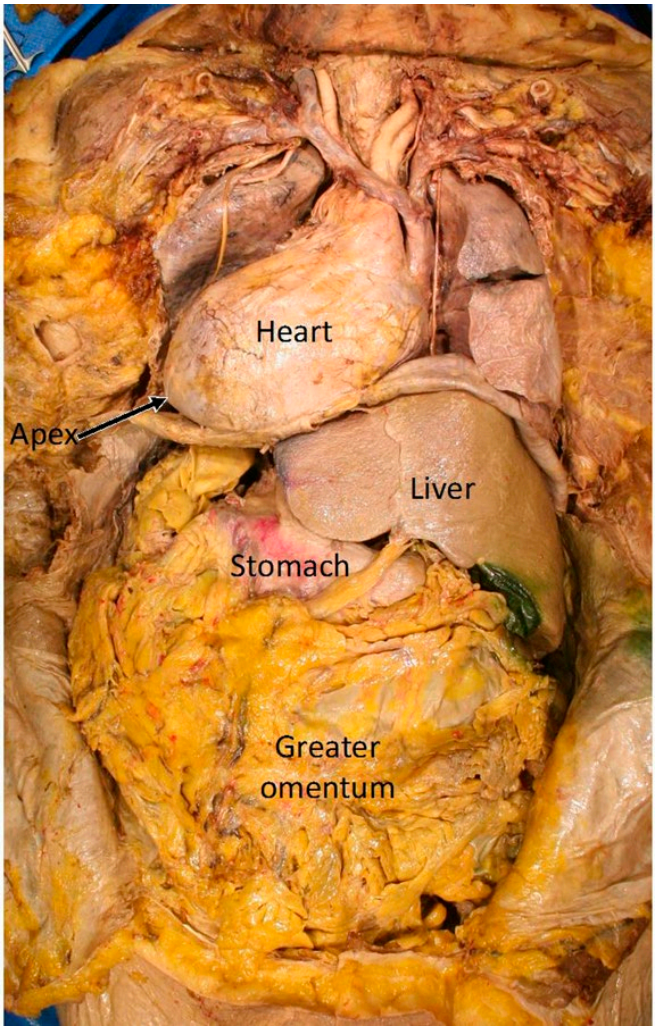

Figure 5. Gross dissection to examine the internal viscera of situs inversus totalis. The apex of the heart is directed to the right (dextrocardia) in the thoracic cavity. The liver is located in the left upper quadrant, and the major part of the stomach is in the right upper quadrant of the abdominal cavity.

of both mesenteric arteries anastomosed to form the marginal artery of Drummond which supplied the large intestines.

In the posterior part of the abdominal cavity, the inferior vena cava was located on the left side of the abdominal aorta. The inferior vena cava traveled superiorly and posteriorly to the liver where the left, middle, and right hepatic veins drained into it. It then passed through the diaphragm at the TV8 level into the thoracic cavity and drained into the left-sided functional right atrium. The kidneys were named by their anatomical position. The right renal artery branched into the apical, anterior

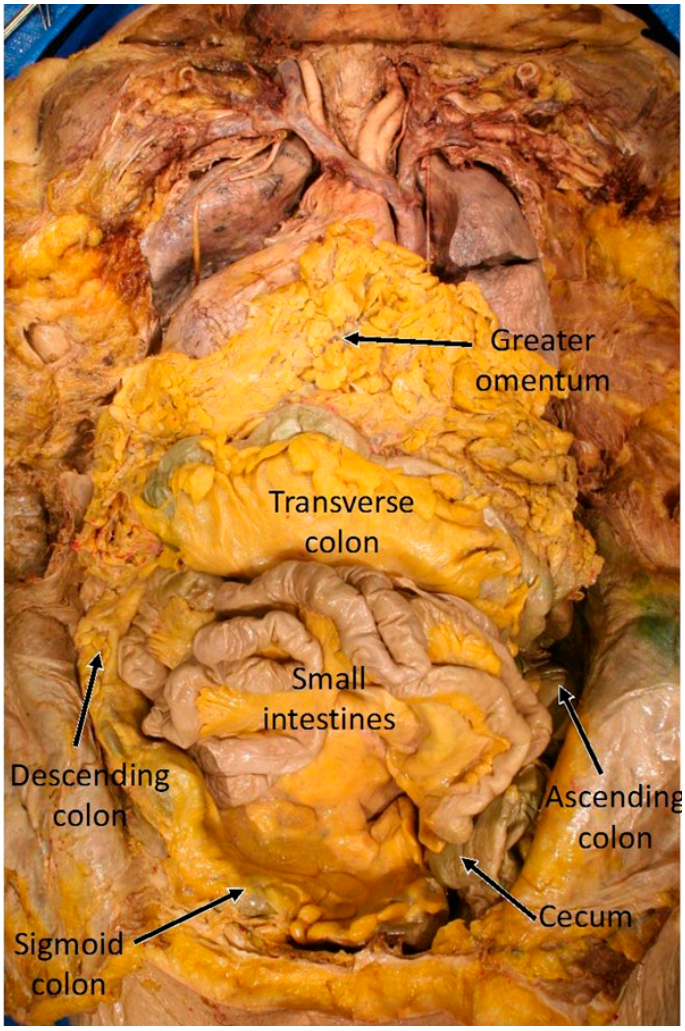

Figure 6. Gross dissection to examine the small and large intestines. The cecum and ascending colon are on the left side, while the descending colon and sigmoid colon are on the right side of the abdomen. The transverse colon travels horizontally from left to right across the abdomen.

superior, anterior inferior, inferior, and posterior renal arteries. Only four branches from the left renal artery were observed and they were the apical, anterior superior, anterior inferior and posterior renal arteries. In this study, the left inferior renal artery branched directly from the abdominal aorta. The right renal vein received a common trunk of the right inferior phrenic vein and suprarenal vein superiorly and the ovarian vein inferiorly, and then passed anterior to the abdominal aorta and posterior to the superior mesenteric artery to drain into the inferior vena cava. The left renal vein drained directly into the left-sided inferior vena cava. Both ovarian arter-

ies branched directly from the abdominal aorta, while the right ovarian vein drained into the right renal vein and the left ovarian vein drained directly into the inferior vena cava (Figs. S17 & S18). Summary of the gross anatomical dissection is presented in the supplementary Tables S1 & S2. Altogether, the results of both the CT imaging and gross anatomical dissection characterize the present case as situs inversus totalis with dextrocardia.

Genetic analysis

The cumulative exome coverage at ≥ 10X depth of coverage was limited to 40.2% due to DNA degradation. In total 19,303 genetic variants were detected. The variants with predicted deleterious (pathological) substitution of amino acids in the mutant proteins were selected through sequential stringent filtering steps that included analysis provided by well established SWIFT (Sim et al., 2012), PolyPhen_2-HDIV (Adzhubei et al., 2010), and PROVEAN (Choi and Chan, 2015) algorithms and servers (Table 1). From the 134 genetic variants predicted to be pathologic (Table S3), seven, *BBS1*, *C5orf42*, *DYNC2H1*, *DVL1*, *DNAH9*, *PKD1* and *TRPV4* could have a negative effect on cilia structure and function thereby leading to the development of situs inversus (Nonaka et al., 1998; Bisgrove and Yost, 2006; Fliegauf et al., 2007; Leigh et al., 2009; Pennekamp et al., 2015). However, the first three genetic variants, *BBS1*, *C5orf42*, and *DYNC2H1,* have been previously linked to several well described human genetic disorders including, respectively, Bardet-Biedl syndrome (Ajmal et al., 2013; Ece Solmaz et al., 2015), oral-facial-digital syndrome VI (Karp et al., 2012), and short-rib polydactyly syndrome (Mei et al., 2015; Okamoto et al., 2015). Because none of the pathologies related to the above syndromes have been identified in the current study, the remaining four variants, *DVL1*, *DNAH9*, *PKD1,* and *TRPV4,* are the ones most likely associated with the development of situs inversus totalis, primarily through the impairment of cilia structure and function (Table 2). All four of these

Table 2. Deleterious (pathologic) genetic variants associated with the current case of situs inversus totalis, that regulate cilia structure and function.

Gene	Protein Function	Variant
DVL1	Dishevelled segment polarity protein 1. Plays a role both in canonical and non-canonical Wnt signaling. Participates in Wnt signaling by binding to the cytoplasmic C-terminus of frizzled family members and transducing the Wnt signal to down-stream effectors.	p.Arg108Trp
DNAH9	Dynein heavy chain 9, axonemal. Force generating protein of respiratory cilia. Produces force towards the minus ends of microtubules.	p.Arg3447His
PKD1	Polycystin-1. Acts as a regulator of cilium length, together with PKD2. The dynamic control of cilium length is essential in the regulation of mechanotransductive signaling.	p.Arg3620Trp p.Arg3621Trp
TRPV4	Transient receptor potential cation channel subfamily V member 4. Non-selective calcium permeant cation channel involved in osmotic and mechanosensitivity. Primary cilia receptor.	p.Leu223Val p.Leu257Val

variants are novel as they have never been linked before to the laterality disorders in humans including situs inversus totalis (Deng et al., 2015).

Discussion

The case of a 96-year old female cadaver presented in the current study can be described as situs inversus totalis with dextrocardia. The latter is a rare condition only seen in 0.01% of the population. Individuals with situs inversus totalis usually have a normal life expectancy and the risk of contracting a disease is similar to that of patients with situs solitus (Kumar et al. 2014). Our description of the present case as situs inversus totalis was based on the completely reversed orientation of the thoracoabdominal viscera which was unequivocally supported by the respective CT imaging data and the anatomical dissection results. In addition, we noted a presence of various minor vascular anomalies within the abdomen that are described below.

In anatomically typical individuals, the celiac trunk usually branches as a triad of three arteries: left gastric artery, splenic artery and common hepatic artery. In the present case, the celiac trunk bifurcated into the splenic artery and left gastric artery. Yet the common hepatic artery and superior mesenteric artery shared a common trunk, and the left gastric artery and an accessory hepatic artery shared a common trunk that branched from the proper hepatic artery. The accessory hepatic artery passed through the hepatoduodenal ligament and traveled with the right hepatic artery to the functional right lobe of the liver. The inferior pancreaticoduodenal artery branched from the common hepatic artery instead of the superior mesenteric artery. Finally, the left inferior renal artery branched directly from the abdominal aorta.

It is well established that cardiac anomalies are common in patients with situs ambiguous, while 90-95% of patients with situs inversus totalis have a typical internal cardiovascular structure (Applegate et al., 1999; Hur et al., 2014), which was observed also in the current study. However, even though the heart structures were reversed as compared to normal anatomy, the morphology of each heart chamber was unremarkable. In addition, the formation of inferior vena cava and azygos vein were also reversed but normal which is unlike other cases of heterotaxy, where the azygos vein being the continuation of the inferior vena cava represents the most common cardiovascular anomaly (Applegate et al., 1999; Maldjian and Saric, 2007; Kumar et al., 2014; Ghorbnazadeh et al., 2017).

In order to gain insights into the etiology of the current case, we performed a screen for the putative genetic variants associated with situs inversus totalis by employing NGS of the DNA extracted from the body used in the current study. The respective bioinformatics analysis identified four most relevant variants, *DNAH9*, *PKD1*, *TRPV4*, and *DVL1*, all of them being involved in the regulation of cilia structure and function. *DNAH9* is a human homolog of mouse *Dnahc9* which encodes a dynein heavy chain 9, an important axonemal component of cilia, and its mutation could lead to the impairment of motile cilia (Thomas et al., 2010; Huang et al., 2015). Earlier studies showed that defects in motile cilia could result in the randomization of the left-right axis during early embryogenesis (Nonaka et al., 1998; Tabin and Vogan, 2003) thereby promoting the development of laterality defects. On the other hand, *PKD1*, *TRPV4*, and *DVL1* genetic variants could be responsible for the impair-

ment of primary cilia function. Studies on *Pkd1*, also known as polycystin-1, demonstrated its close involvement in the mechanosensation coupled with the intracellular calcium signaling in the primary kidney cilia where it co-distributes and functions in the same mechanotransduction pathway with polycystin-2 (*Pkd2*) (Nauli et al., 2003). More importantly, it has been also reported that *Pkd2* deficient mice displayed a complex spectrum of laterality defects (Yoshiba et al. 2012). *TRPV4* encodes a human homolog of mouse *Trpv4*, a well-characterized cation channel known to be involved in mechanosensation by serving as one of the receptors of primary cilia (Thomas et al., 2010; Lee et al., 2015). It is also well-established that *DVL1* regulates Wnt signaling which utilizes primary cilia as a signaling platform (Simons et al., 2005; Lancaster et al., 2011; McMurray et al., 2013; Oh and Katsanis, 2013).

In summary, the results of our genetic analysis could provide evidence in support of the two-cilia model where both motile primary and non-motile primary cilia work synergistically at the node to initiate the asymmetrical Nodal cascade in the left lateral plate mesoderm (McGrath et al., 2003; Nauli et al., 2003; Yoshiba and Hamada, 2014; Duncan and Khokha, 2016). However, it appears that the disruption of both the motile primary and non motile primary cilia could be a prerequisite for the development of situs inversus totalis described in the present case. In the latter, the disruption of motile primary cilia could be linked to *DNAH9* mutation and the impairment of non-motile primary cilia may result from the mutations in *PKD1*, *TRPV4*, and *DVL1*.

In conclusion, it should be noted that the genetic analysis of human pathologies or anatomical aberrations can only reveal an association of a specific genetic variation(s) with the observed phenotypical changes. A causative link between the particular genotypic and phenotypic changes can only be established by reproducing the latter through either the respective genetic manipulations in the model organisms (systems) or by correcting an existing pathology by targeting a transcription of a mutated gene(s) or the respective protein function. Nevertheless, the associative (in general) nature of genetic analysis, including that presented in the current report, could provide invaluable leads in unraveling new molecular mechanisms governing the development of a human organism, including asymmetrical patterning of visceral organs.

Acknowledgements

We gratefully acknowledge Mr. Todd Gebke (SLU Hospital) for his expert assistance with CT imaging and Dr. Paul Cliften (GTAC, Washington University in St. Louis) for his invaluable help with the bioinformatics analysis.

This study was supported by the Center for Anatomical Science and Education, SLU School of Medicine.

No competing interest have to be declared.

These data were presented in part at the Annual Experimental Biology Meeting (FASEB J. (2018), 32: Suppl.1, Abstract 89.4).

Additional information

Supplementary materials are available through: https://drive.google.com/file/d/1x2LXQeRrlyCIxmElO_U7mQdHPfDzyxhv/view

References

Adzhubei I.A., Schmidt S., Peshkin L., Ramensky V.E., Gerasimova A., Bork P., Kondrashov A.S., Sunyaev S. R. (2010). A method and server for predicting damaging missense mutations. Nat. Methods 7: 248-249.

Ajmal M., Khan M.I., Neveling K., Tayyab A., Jaffar S., Sadeque A., Ayub H., Abbasi N.M., Riaz M., Micheal S., Gilissen C., Ali S.H., Azam M., Collin R.W., Cremers F.P., Qamar R. (2013). Exome sequencing identifies a novel and a recurrent BBS1 mutation in Pakistani families with Bardet-Biedl syndrome. Mol. Vis. 19: 644-653.

Applegate K.E., Goske M.J., Pierce G., Murphy D. (1999). Situs revisited: imaging of the heterotaxy syndrome. Radiographics 19: 837-852.

Bisgrove B.W., Yost H.J. (2006). The roles of cilia in developmental disorders and disease. Development 133: 4131-4143.

Blum M., Feistel K., Thumberger T., Schweickert A. (2014). The evolution and conservation of left-right patterning mechanisms. Development 141: 1603-1613.

Burton E.C., Olson M., Rooper L. (2014). Defects in laterality with emphasis on heterotaxy syndromes with asplenia and polysplenia: an autopsy case series at a single institution. Pediatr. Dev. Pathol. 17: 250-264.

Casey G., Campeau L. (2014). Video documentary of situs inversus totalis in a male cadaver module 1 to 5. MedEdPORTAL. 10: 9817 (doi: 10.15766/mep_2374-8265.9817), 9980 (doi: 10.15766/mep_2374-8265.9980), 9833 (doi: 10.15766/mep_2374-8265.9833), 9812 (doi: 10.15766/mep_2374-8265.9812), 9814 (doi: 10.15766/mep_2374-8265.9814).

Choi Y., Chan A.P. (2015). PROVEAN web server: a tool to predict the functional effect of amino acid substitutions and indels. Bioinformatics 31: 2745-2747.

Delton A. (2017). Grant's Dissector. 16th edn. Wolters Kluwer, Philadelphia. Pp. 77-136.

Deng H., Xia H., Deng S. (2015). Genetic basis of human left-right asymmetry disorders. Expert Rev. Mol. Med. 16: e19.

Duncan A.R., Khokha M.K. (2016). Xenopus as a model organism for birth defects-Congenital heart disease and heterotaxy. Semin. Cell Dev. Biol. 51: 73-79.

Ece Solmaz A., Onay H., Atik T., Aykut A., Cerrah Gunes M., Ozalp Yuregir O., Bas V.N., Hazan F., Kirbiyik O., Ozkinay F. (2015). Targeted multi-gene panel testing for the diagnosis of Bardet Biedl syndrome: Identification of nine novel mutations across BBS1, BBS2, BBS4, BBS7, BBS9, BBS10 genes. Eur. J. Med. Genet. 58: 689-694.

Ekbote A.V., Kamath M.S., Danda S. (2014). MURCS association with situs inversus totalis: Expanding the spectrum or a novel disorder. J. Pediatr. Genet. 3: 167-173.

Elder C.T., Metzger R., Arrington C., Rollins M., Scaife E. (2014). The role of screening and prophylactic surgery for malrotation in heterotaxy patients. J. Pediatr. Surg. 49: 1746-1748.

Fliegauf M., Benzing T., Omran H. (2007). When cilia go bad: cilia defects and ciliopathies. Nat. Rev. Mol. Cell Biol. 8: 880-893.

Frolov A., Tan Y., Rana M., Martin J.R. 3rd (2018). A rare case of human diphallia associated with hypospadias. Case Rep. Urol. 2018: 8293036 [6 pages].

Ghorbnazadeh A., Zirak N., Fazlinezhad A., Moenipour A., Manshadi H.H., Teshnizi M.A. (2017). Situs inversus with levocardia and congenitally corrected transposition of great vessels in a 35 year old male: a case report. Electron. Physician 9: 3570-3574.

Huang B.K., Gamm U.A., Jonas S., Khokha M.K., Choma M.A. (2015). Quantitative optical coherence tomography imaging of intermediate flow defect phenotypes in ciliary physiology and pathophysiology. J. Biomed. Opt. 20: 030502.
Hur M.-S., Chung I.-H., Lee K.-S. (2014). Dextracardia and situs inversus with incomplete inversion: a case report. Korean J. Phys. Anthropol. 27: 173-178.
Karp N., Grosse-Wortmann L., Bowdin S. (2012). Severe aortic stenosis, bicuspid aortic valve and atrial septal defect in a child with Joubert Syndrome and Related Disorders (JSRD) - a case report and review of congenital heart defects reported in the human ciliopathies. Eur. J. Med. Genet. 55: 605-610.
Kim S.J. (2011). Heterotaxy syndrome. Korean Circ. J. 41: 227-232.
Kumar A., Singh M.K., Yadav N. (2014). Dextrocardia and asplenia in situs inversus totalis in a baby: a case report. J. Med. Case Rep. 8: 408.
Lancaster M.A., Schroth J., Gleeson J.G. (2011). Subcellular spatial regulation of canonical Wnt signalling at the primary cilium. Nat. Cell Biol. 13: 700-707.
Lee K.L., Guevarra M.D., Nguyen A.M., Chua M.C., Wang Y., Jacobs C.R. (2015). The primary cilium functions as a mechanical and calcium signaling nexus. Cilia 4: 7.
Leigh M.W., Pittman J.E., Carson J.L., Ferkol T.W., Dell S.D., Davis S.D., Knowles M.R., Zariwala M.A. (2009). Clinical and genetic aspects of primary ciliary dyskinesia/Kartagener syndrome. Genet. Med. 11: 473-487.
Lin A.E., Krikov S., Riehle-Colarusso T., Frias J.L., Belmont J., Anderka M., Geva T., Getz K.D., Botto L.D., National Birth Defects Prevention Study (2014). Laterality defects in the national birth defects prevention study (1998-2007): birth prevalence and descriptive epidemiology. Am. J. Med. Genet. A. 164A: 2581-2591.
Maldjian P.D., Saric M. (2007). Approach to dextrocardia in adults: review. Am. J. Roentgenol. 188: S39-S49.
McGrath J., Somlo S., Makova S., Tian X., Brueckner M. (2003). Two populations of node monocilia initiate left-right asymmetry in the mouse. Cell 114: 61-73.
McMurray R.J., Wann A.K., Thompson C.L., Connelly J.T., Knight M.M. (2013). Surface topography regulates wnt signaling through control of primary cilia structure in mesenchymal stem cells. Sci. Rep. 3: 3545.
Mei L., Huang Y., Pan Q., Su W., Quan Y., Liang D., Wu L. (2015). Targeted next-generation sequencing identifies novel compound heterozygous mutations of DYNC2H1 in a fetus with short rib-polydactyly syndrome, type III. Clin. Chim. Acta 447: 47-51.
Nauli S.M., Alenghat F.J., Luo Y., Williams E., Vassilev P., Li X., Elia A.E., Lu W., Brown E.M., Quinn S.J., Ingber D.E., Zhou J. (2003). Polycystins 1 and 2 mediate mechanosensation in the primary cilium of kidney cells. Nat. Genet. 33: 129-137.
Nonaka S., Tanaka Y., Okada Y., Takeda S., Harada A., Kanai Y., Kido M., Hirokawa N. (1998). Randomization of left-right asymmetry due to loss of nodal cilia generating leftward flow of extraembryonic fluid in mice lacking KIF3B motor protein. Cell 95: 829-837.
Oh E.C., Katsanis N. (2013). Context-dependent regulation of Wnt signaling through the primary cilium. J. Am. Soc. Nephrol. 24: 10-18.
Okamoto T., Nagaya K., Kawata Y., Asai H., Tsuchida E., Nohara F., Okajima K., Azuma H. (2015). Novel compound heterozygous mutations in DYNC2H1 in a patient with severe short-rib polydactyly syndrome type III phenotype. Congenit. Anom. (Kyoto) 55: 155-157.

Pennekamp P., Menchen T., Dworniczak B., Hamada H. (2015). Situs inversus and ciliary abnormalities: 20 years later, what is the connection? Cilia 4: 1.

Sim N.L., Kumar P., Hu J., Henikoff S., Schneider G., Ng P.C. (2012). SIFT web server: predicting effects of amino acid substitutions on proteins. Nucleic Acids Res. 40: W452-W457.

Simons M., Gloy J., Ganner A., Bullerkotte A., Bashkurov M., Krönig C., Schermer B., Benzing T., Cabello O., Jenny A, Mlodzik M., Polok B., Driever W., Obara T., Walz G. (2005). Inversin, the gene product mutated in nephronophthisis type II, functions as a molecular switch between Wnt signaling pathways. Nat. Genet. 375: 537-543.

Tabin C.J., Vogan K.J. (2003). A two-cilia model for vertebrate left-right axis specification. Genes Dev. 17: 1-6.

Thomas J., Morle L., Soulavie F., Laurencon A., Sagnol S., Durand B. (2010). Transcriptional control of genes involved in ciliogenesis: a first step in making cilia. Biol. Cell 102: 499-513.

Vandenberg L.N., Levin M. (2013). A unified model for left-right asymmetry? Comparison and synthesis of molecular models of embryonic laterality. Dev. Biol. 379: 1-15.

Weir J., Abrahams P.H., Spratt J.D., Salkowski L. (2011). Imaging Atlas of Human Anatomy. Mosby, Edinburgh.

Yoshiba S., Hamada H. (2014). Roles of cilia, fluid flow, and Ca2+ signaling in breaking of left-right symmetry. Trends Genet. 30: 10-17.

Yoshiba S., Shiratori H., Kuo I.Y., Kawasumi A., Shinohara K., Nonaka S., Asai Y., Sasaki G., Belo J.A., Sasaki H., Nakai J., Dworniczak B., Ehrlich B.E., Pennekamp P., Hamada H. (2012). Cilia at the node of mouse embryos sense fluid flow for left-right determination via Pkd2. Science 338: 226-231.